Biointerface Research in Applied Chemistry
Open-Access Journal (ISSN: 2069-5837)

Article
Volume 13, Issue 2, 2023, 179
https://doi.org/10.33263/BRIAC132.179

Synthesis and Characterization of Sn-Doped CeO_2-Fe_2O_3 Nanocomposite and Application in Photocatalytic Degradation of Sudan I

Shiv Alwera [1], Vladimir Sergeevich Talismanov [2], Vijay Alwera [1,*], Doaa Domyati [3]

[1] Department of Chemistry, Indian Institute of Technology Roorkee, 247667, Uttarakhand, India
[2] Department of Chemistry, Moscow Institute of Physics and Technology, Dolgoprudny, Moscow Region, 141701, Russian Federation
[3] Department of Chemistry, College of Science, University of Jeddah, P.O. Box 80327, Jeddah 21589, Saudi Arabia
* Correspondence: alweravijay@gmail.com (S.A.);

Scopus Author ID 57216541551
Received: 31.01.2022; Accepted: 10.03.2022; Published: 30.03.2022

Abstract: Photocatalysis is a promising technique to treat organic dyes as pollutants over traditional technologies. The application of organic dyes has increased lately for industries such as textile, medicines, plastics, etc. Thus, in this report, we prepared a Tin-doped CeO_2-Fe_2O_3 photocatalyst via the thermal decomposition method to effectively degrade Sudan I under sunlight. The synthesized catalyst was explored by different studies such as powder X-ray diffraction (XRD), field-emission scanning electron microscopy (FE-SEM), Brunauer-Emmett-Teller (BET), UV-vis diffuse reflectance (UV-vis DRS). The catalyst was found to have a particle size of 1-2 µm with a high surface area. The bandgap energy of the catalyst was changed to 2.2 eV due to the Sn doping. The effect of Sn^{4+} doping into the CeO_2 lattice was observed as the modification in the Fermi levels of the catalyst, which resulted in enhanced photocatalytic activity. The catalyst was found to have a fast degradation rate towards Sudan I under the sunlight and showed complete degradation. The result of COD removal confirmed the removal of dye from the dye solution. Further, scavenger tests confirmed the role of the active species, hydroxyl ($^{\bullet}OH$) and superoxide ($O_2^{\bullet-}$) radicals, in the degradation of Sudan I by photocatalyst. High-performance liquid chromatography (HPLC) was used to confirm the complete degradation of the dye. A possible mechanism is put forward to describe the degradation process and charge transfer during the degradation.

Keywords: metal oxides; photocatalyst; degradation; Sudan I; HPLC; COD.

1. Introduction

In recent years, the development of industries has grown very fast to serve human needs. Even if this development is essential, it is still causing an alarming situation for humans and living kind due to the continuous release of pollutants into the water and environment [1]. The pollutants released from the industries are oils, pharmaceuticals, radioactive waste, cosmetics, photochemical, textiles discharge, etc., which causes pollution of drinking water, groundwater, and rivers, one of our major problems [2]. According to the World Health Organization (WHO) report, 2018, around 800 million people do not have basic access to drinking water [3], which is a major problem.

One of the industrial wastes is organic dyes which are commonly used in textile, leather, paint, food, cosmetics industries, etc. The organic dyes are harmful to animals, aquatic species,

plants, and humans due to their carcinogenic and mutagenic effects [2,4]. Approximately hundreds of dyes are commercially used in different industries, including azo dyes such as Acid Orange, Acid Red, Methyl Orange, methyl red, basic red, Sudan I-IV, Sudan red, etc. Among these dyes, Sudan I, known as Cl solvent yellow 14 and solvent orange R, is used to color waxes, oils, petrol, hydrocarbon solvents, polishes, and cosmetics. Sudan I is also used to color many foodstuffs such as curry powder and chili powder [5,6]. Nowadays, many countries have banned Sudan I in foods because Sudan I, Sudan III, and Sudan IV have been classified as a category-3 carcinogen by the International Agency for Research on cancer and a suspect of causing genetic defects. Apart from this, Sudan I caused allergic skin reactions and skin irritation [7]. Therefore, it is necessary to treat the dye contained in polluted water to get clean water. For this, several methods are available to treat polluted water, such as chemical, physical, etc. Traditional water treatment methods such as coagulation, membrane filtration, reverse osmosis, etc., are not effective in removing organic dyes [8]. So, there are many technologies being developed by researchers to degrade and remove such dyes. These technologies include chlorination, electrochemical oxidation, ozonation, bio-degradation, adsorption, photocatalytic degradation, etc., but photocatalytic degradation is considered one of the best methods for dye degradation [8-13]. For a compound to show the photocatalytic property, it should be a semiconductor with a sufficient band gap to degrade dyes, e.g., metal oxides, nitrides, sulfides [14-20]. For example, metal oxides such as TiO_2, ZnO, CuO, CeO_2, Fe_3O_4, Fe_2O_3, $BiVO_4$ are widely used due to their photocatalytic, catalytic activity, energy storage, water splitting properties [21-26].

A photocatalyst compound should have the following properties such as suitable band gap values, charge transfer efficiency, less photo-corrosion. Generally, the efficiency of a photocatalyst is limited by the large band gaps and low charge transfer values. Thus a photocatalyst needs to be designed to overcome these drawbacks. For this purpose, hetero-junctions are introduced into the photocatalyst system by doping metals or non-metals, which reduces the bandgap energies and increases the charge transfer efficiency [27,28]. Many researchers are interested in fluorite structured CeO_2 metal oxide systems due to their high efficiency in solar cells, fuel cells, sensors, and high thermal-chemical stability [29,30]. But CeO_2 has a large bandgap of 3.2 eV, which does not show photocatalytic activity under sunlight. So, to overcome this situation, CeO_2 is mixed or doped with different metals or metal oxides such as CeO_2-TiO_2, CeO_2-Bi_2O_3, CeO_2-$BiVO_4$, CeO_2-Cu_2O, CeO_2-ZnO, CeO_2-α-MoO_3, CeO_2-ZnO-TiO_2 [25,31-33]. The bandgap of CeO_2 can be decreased by doping a metal oxide that already has a lower bandgap value, for example, Fe_2O_3, which has a low bandgap with high visible light absorptivity [34,35].

Therefore, we tried to synthesize a mixed metal oxide compound that is active for dye degradation under sunlight. In this report, CeO_2 is mixed and doped with Fe_2O_3 and Sn^{4+} metal ion where Sn^{4+} occupies Ce^{4+} sites and causes the modification in band position with enhanced charge separation. The Sn^{4+} doped CeO_2-Fe_2O_3 composite system is designed for high visible light absorptivity and high charge concentration at the catalyst surface [36,37]. The synthesized catalyst was studied by XRD, FESEM for the phase and structural properties. The textural properties and the surface area were measured by BET analysis. The photocatalytic degradation of Sudan I by CeO_2-Fe_2O_3 and Sn doped CeO_2-Fe_2O_3 catalysts revealed that Sn doped CeO_2-Fe_2O_3 catalyst was found to be more active towards the degradation of Sudan I. Further, the effect of doses and pH on photocatalytic degradation was studied, and the reusability of the catalyst was studied by performing a cyclic test. The scavenger study was carried out to

understand the photocatalytic process and proposed a plausible mechanism. The presence of intermediate molecules was identified by HPLC analysis [38,39].

2. Materials and Methods

2.1. Chemicals and reagents.

$FeCl_3$, $Ce(NO_3)_2.6H_2O$, and $SnCl_4.5H_2O$ of analytical grade were purchased from Sigma-Aldrich. Sudan I dye, Sodium hydroxide (NaOH), hydrochloric acid (HCl) were purchased from Alfasar. HPLC grade Acetonitrile was purchased from E. Merck.

2.2. Synthesis method.

The synthesis of Sn-doped CeO_2-Fe_2O_3 composite is followed by a thermal decomposition method. For this purpose, $FeCl_3$ and $Ce(NO_3)_2.6H_2O$ were taken in a 1:2 molar ratio, and $SnCl_4.5H_2O$ was used 5% of the total mass. After this, all chemicals were dispersed in isopropanol solvent (100 mL). Then, the mixture was stirred magnetically on a magnetic stirrer at 85 °C. After it got dry, a powder was obtained, which was further heated for 1 h at 120 °C in a vacuum oven. After this, the compound was grounded in a mortar pestle for 1 h for proper mixing and then placed in a muffle furnace for 2 h at 450 °C for calcination [34,40,41]. The obtained compounds were then studied for their photocatalytic activity.

2.3. Photocatalytic activity experiment.

The photocatalytic activity of the compounds was tested in the month of April to July under the sunlight. For this, 100 mg of catalyst was mixed with 100 mL of dye solution (1×10^{-5} M), in a 250 mL beaker. The pH of the dye solutions was adjusted by adding dil. HCl and NaOH to the dye solution. Then the dye and catalyst solution was stirred for 3 h to establish the adsorption-desorption equilibrium, and then the beaker was placed under direct sunlight. After a certain time, 3 mL of aliquots were collected from the beaker and recorded the change in the dye concentration. For this, the aliquots were first centrifuged at 10,000 rpm, and then the UV-vis spectrum was recorded. The degradation efficiency of the catalyst was calculated according to the following equation.

$$\text{Degradation Efficiency} = \frac{C_0 - C}{C_0} \times 100$$

where C_0 and C denote the initial and final absorbance of the dye solutions [35]. After the photocatalytic experiment, the used catalyst was recovered for the next cycle for up to three consecutive cycles.

2.4. Characterization.

The X-ray powder diffraction (XRD) was recorded by using a Bruker AXSD8 Advance diffractometer (Cu-Kα1; l = 1.5406 Å). Field emission scanning electron microscopy (FESEM) was recorded by using Zeiss, Ultra plus55. Brunauer-Emmett-Teller (BET) surface area measurement of the compound was performed by using NOVA 2200e instrument. The pH of the dye solutions was measured by a pH meter (Eutech pH 700).

The Diffuse Reflectance Spectra (DRS) were recorded on the Shimadzu UV-2450 spectrophotometer within 200-800 nm wavelength. The reflectance data were converted to absorption according to the Kubelka-Munk (K-M) theory-

$$F(R_\infty)=(1-R_\infty)^2/2R_\infty$$

where R_∞ is the reflectance of the sample and $F(R_\infty)$ is the K-M function. The bandgap of the samples was calculated by Tauc Plot by using the following equation-

$$(\alpha h\nu)^{1/n} = A(h\nu-E_g)$$

where α, $h\nu$, A, and E_g are the absorption coefficient, incident light frequency, proportionality constant, and bandgap, respectively. The value of n = 2 for indirect transition.

2.5. Chemical Oxygen Demand (COD).

COD of the dye solution was measured by using a digestion unit (DRB 200) and UV-vis spectrophotometer. After a certain time interval, the sample aliquots were collected for the COD analysis and centrifuged at 10,000 rpm for 10 minutes. The photocatalytic degradation efficiency from the COD results was calculated by using the following equation:

$$\text{Photodegradation efficiency} = \frac{\text{initial COD} - \text{final COD}}{\text{initial COD}} \times 100$$

2.6. High-Performance Liquid Chromatography (HPLC).

HPLC analysis was done by using Shimadzu LC-2010AHT (PDA detector) along with the C_{18} column [38]. Acetonitrile and water (1:1), H_3PO_4 (50mM) at 3.5 pH were used as the mobile phase and operated in gradient mode [39]. The HPLC was recorded by collecting 3 mL reaction aliquots were collected after a time interval. The sample aliquots were first centrifuged in order to remove the catalyst particles and then filtered through a 45 μm syringe filter.

2.7. Detection of reactive species.

The scavenger tests were performed to detect and identify the involved reactive species in the photocatalytic reaction. For this purpose, scavengers such as benzoquinone (BQ) for $O_2^{\bullet-}$, ammonium oxalate (AO) for h^+, and tert-butanol (*t*-BuOH) for $^\bullet OH$ scavenging are used. A suitable scavenger (1 mM) was added to the catalyst-dye solution, and similar photocatalytic experiments were performed.

3. Results and Discussion

3.1. Characterization.

3.1.1. XRD analysis.

The Sn-doped CeO_2-Fe_2O_3 composite was identified by using X-ray powder diffraction. Figure 1(i) represents the XRD patterns of Sn-doped CeO_2-Fe_2O_3 and un-doped CeO_2-Fe_2O_3. Here, Figure 1(i-a) shows the XRD patterns for CeO_2-Fe_2O_3 and the peaks obtained at 2θ = 27.2, 28.99, 33.39, 47.91, 56.75, 69.6, 79.47 represent the (012), (111), (200), (220), (311), (400) and (420) planes, respectively. These planes confirmed the formation of the phase of CeO_2 with fluorite structure [JCPDS# 00-034-0394] [42].

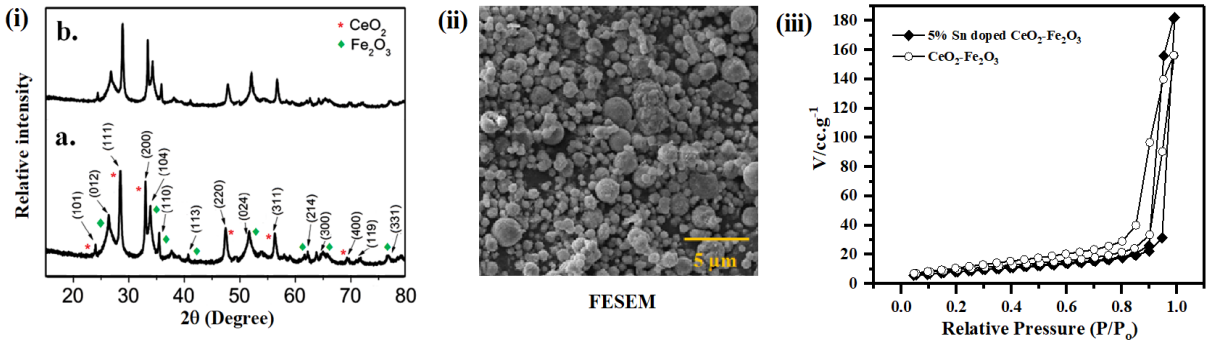

Figure 1. (**i**) XRD pattern for **a**) CeO_2-Fe_2O_3, and **b**) Sn doped CeO_2-Fe_2O_3 composite. (**ii**) The BET surface area of CeO_2-Fe_2O_3 and Sn doped CeO_2-Fe_2O_3 composites and FESEM image is shown in the inbox.

While the remaining XRD peaks at 25.1, 35.4, 49.7, 54.9, and 62.1 represent the (101), (110), (024), (116), and (214) crystal planes, respectively, and belong to the rhombohedral phase of Fe_2O_3 [40]. The XRD pattern is shown in Figure 1(i-b) has a similar XRD pattern as CeO_2-Fe_2O_3 with a slight shift in 2θ values. The similarity in the XRD peaks indicates the incorporation of doped Sn^{4+} into the structure. But the shift in peaks position towards high 2θ values compared to the un-doped CeO_2-Fe_2O_3 sample is found due to the interaction of Sn^{4+} with Ce and Fe in the crystal structure. The Sn^{4+} forms SnO_2 after replacing Ce^{4+} from the CeO_2 lattice to form Sn doped CeO_2 lattice. This Sn-doped CeO_2 lattice interacted with Fe_2O_3, which caused the shift towards higher 2θ values.

3.1.2. Surface analysis.

Next, the textural properties of Sn doped CeO_2-Fe_2O_3 composite were studied to analyze the morphology of the catalyst. Figure 1(ii and iii) show the FESEM and BET analysis of Sn doped CeO_2-Fe_2O_3 composite. The FESEM image shows hierarchical sphere-shaped morphology with a rough-textured surface, and the particle size of spheres varies in the range of 1-2 µm. The surface area of the catalyst was investigated by BET analysis, and a typical N_2 adsorption-desorption isotherm curve is shown in Figure 1(iii). The Figure shows that both catalysts have a typical type IV isotherms curve [43]. The surface area of Sn doped and undoped CeO_2-Fe_2O_3 catalyst was found 24.2 and 17.4 m^2/g, respectively. The BET analysis results show the CeO_2-Fe_2O_3 catalyst has very less surface area than Sn doped catalyst.

3.1.3. DRS analysis.

The UV-visible DRS spectra for the CeO_2-Fe_2O_3 and Sn doped CeO_2-Fe_2O_3 composites are shown in Figure 2. Figure 2a is UV-visible absorbance spectra which show a wide absorption edge in the visible region for both catalysts, and the absorption edge appeared above 400 nm [44,45,46]. The CeO_2-Fe_2O_3 composite has shown strong absorption around 500 nm, which further narrowed near 600 nm, while it was not the case for Sn^{4+} doped composite. In the case of the Sn^{4+} doped sample, it showed a high absorption edge around 600 nm, which was found to shift toward high wavelength region than the undoped CeO_2-Fe_2O_3. The significantly high absorption edge of the Sn doped CeO_2-Fe_2O_3 composite is responsible for the high absorptivity of the visible light and results in a high degradation rate. The Tauc plot (Figure 2b) shows the bandgap energy values of the Sn doped and undoped samples. The direct bandgap values for CeO_2-Fe_2O_3 and Sn doped CeO_2-Fe_2O_3 composite was found 2.4 eV and

2.21 eV, respectively. The incorporation of Sn^{4+} into the crystal structure of CeO_2-Fe_2O_3 leads to a decrease in the bandgap, which is favorable for the absorption of visible light.

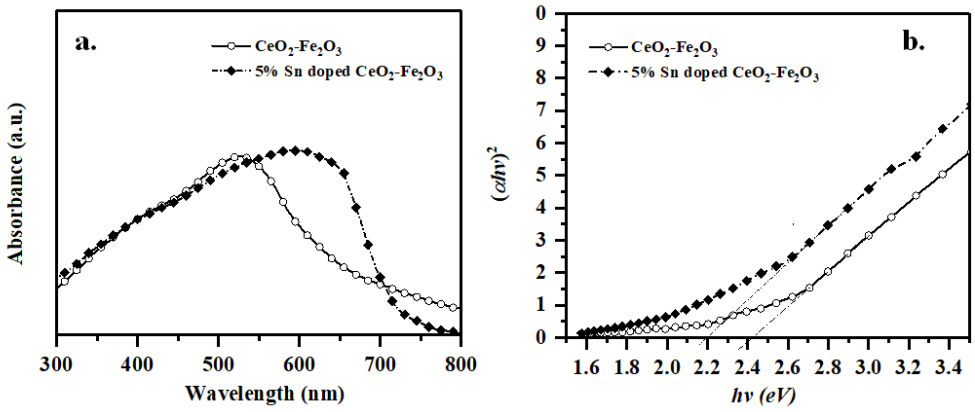

Figure 2. DRS studies, (**a**) UV-visible absorbance spectra; (**b**) Tauc plot for CeO_2-Fe_2O_3 and Sn doped CeO_2-Fe_2O_3.

3.2. Photocatalytic degradation of Sudan I.

For the photocatalytic degradation study, Sudan I (pH= 10) was used as an organic pollutant, and both catalysts, Sn doped CeO_2-Fe_2O_3 and CeO_2-Fe_2O_3 compounds, were tested under sunlight irradiance.

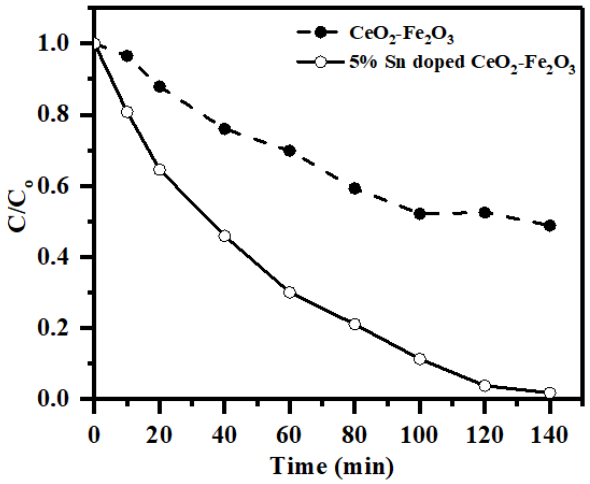

Figure 3. Photocatalytic degradation of Sudan I by CeO_2-Fe_2O_3 and Sn doped CeO_2-Fe_2O_3 as a function of time.

The photocatalytic degradation efficiency of the Sn doped CeO_2-Fe_2O_3 and CeO_2-Fe_2O_3 compounds are shown in Figure 3. The Figure shows that the Sn doped CeO_2-Fe_2O_3 catalyst can degrade approximately 98 % of Sudan I solution within 140 minutes, but the CeO_2-Fe_2O_3 compound can degrade 58 % of Sudan I. The Sn doped CeO_2-Fe_2O_3 has shown a high degradation of Sudan I because it has lower bandgap values than the CeO_2-Fe_2O_3 sample.

3.2.1. Effect of catalyst doses.

The degradation of Sudan I with Sn doped CeO_2-Fe_2O_3 catalyst under sunlight was then studied by the effect of catalyst doses (Figure 4) [47]. For this study, the concentration of Sudan I dye was kept constant (1×10^{-5} M), and the catalyst concentration varied from 0.5 to 1.5 g/L. Figure 4 showed that when the catalyst concentration was 0.5 g/L, only 55 % degradation of Sudan I dye was observed in 140 minutes.

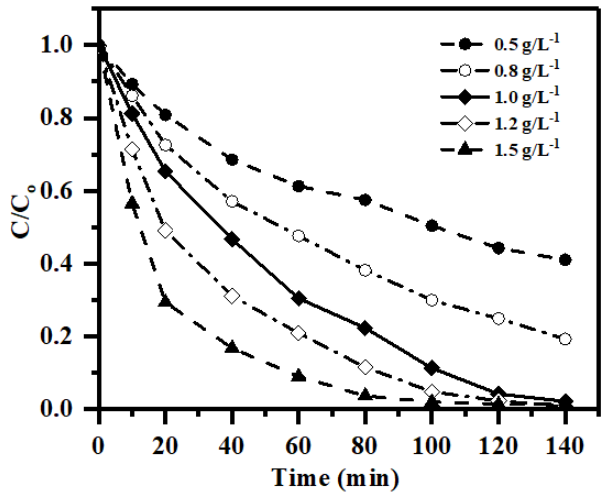

Figure 4. Photocatalytic degradation of Sudan I when the doses of Sn doped CeO_2-Fe_2O_3 catalyst was varied from 0.5 to 1.5 g/L.

Later, as the catalyst concentration was increased, the degradation of Sudan I also increased. For example, 0.8 and 1.0 g/L of catalyst degrades 79 % and 99 % of Sudan I, respectively, and with catalyst concentrations of 1.2 and 1.5 g/L, 99 % degradation was observed within 100 and 80 minutes, respectively. These results show the increase in the catalyst concentration leads to the higher degradation of Sudan I dye, which proves the rate of the degradation of Sudan I is directly proportional to the catalyst concentration.

3.2.2. Effect of pH.

After that, the effect of the pH on the degradation of Sudan I dye by Sn doped CeO_2-Fe_2O_3 catalyst was studied. For this experiment, the concentration of dye and catalyst was kept constant, 1×10^{-5} M and 1.0 g/L, respectively, but the pH of the dye solution was changed from pH 2 to 10.

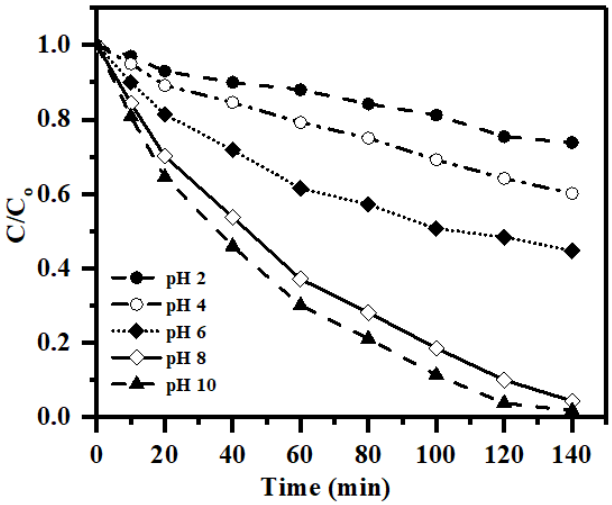

Figure 5. The photocatalytic degradation of Sudan I with Sn doped CeO_2-Fe_2O_3 when the pH of the dye solution varied from pH 2 to 10.

Figure 5 shows the change in the rate of the degradation of Sudan I dye with Sn doped CeO_2-Fe_2O_3 as a function of pH. The Figure showed when the pH of the dye solution was 2, then only 20 % of the dye degraded, and when the pH of the dye solution was varied between 4 and 6, then the degradation reached up to 35% and 52%, respectively. But as the pH of the

dye solution increased to pH 10, the maximum degradation was observed, up to 99 % [48,49]. These results showed that the degradation efficiency is directly proportional to the basic pH of the dye solution.

3.2.3. COD analysis.

Further, the complete degradation and removal of Sudan I from the dye solution were studied by performing a COD removal test. Figure 6 represents the typical graph for the COD removal of Sudan I with Sn doped CeO_2-Fe_2O_3. The graph showed that no COD removal was observed when the catalyst was not added to the dye solution. But as the catalyst was added to the dye solution, the COD removal started, i.e., after 10 minutes, 17 % of COD was removed from the dye solution [43]. After 20 and 40 minutes, the COD of the reaction was removed up to 23 and 40 %, respectively. As the reaction progressed, the COD of the reaction was continuously removed from the solution and recorded up to 98 % at the end of the reaction. So, the COD removal supports the degradation of Sudan I dye with Sn doped CeO_2-Fe_2O_3 catalyst.

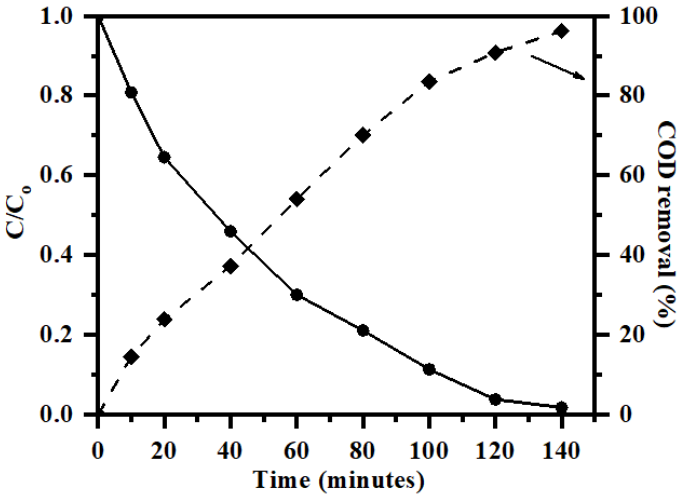

Figure 6. The degradation and COD removal of Sudan I from the dye solution by using Sn doped CeO_2-Fe_2O_3 under sunlight.

3.2.4. HPLC analysis.

After this, the HPLC analysis was performed to ensure the complete degradation and removal of Sudan I by Sn doped CeO_2-Fe_2O_3 catalyst [49-51].

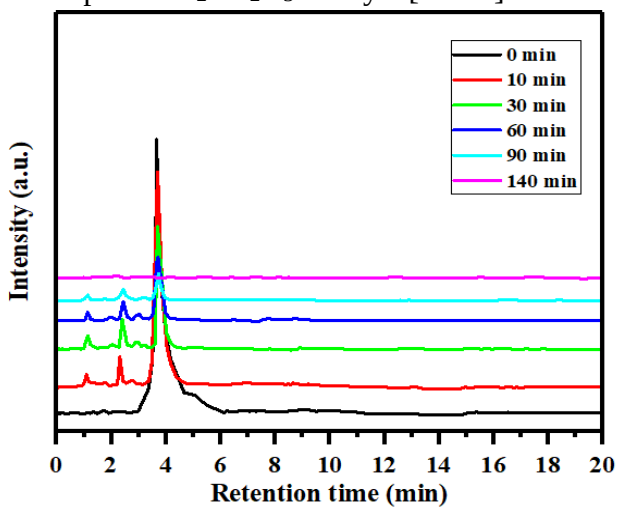

Figure 7. HPLC chromatogram of the degradation of Sudan I from the dye solution with Sn doped CeO_2-Fe_2O_3 under sunlight.

Figure 7 represents the typical HPLC chromatogram for the photocatalytic degradation of Sudan I under sunlight. The chromatograms were recorded at different time intervals, from 0 to 140 min of the reaction. The figure shows the chromatogram at 0 min has a sharp peak at 3.9 min, which corresponds to the characteristic peak for Sudan I.

Then, as the reaction proceeded further, the peak that appeared at 3.9 min started to diminish, showing the degradation of the dye. Later, the peak continues to decrease in the following next chromatograms, and at 140 min, the characteristic peak is about to diminish from the chromatogram.

The removal of the peak at 3.9 min from the chromatogram represents the degradation of Sudan I from the dye solution. On the other hand, the new peaks are seen at 1.2, 1.8, 2.4, 2.8, and 3.1 min in the chromatogram presented at 10 min. These new peaks represent the degraded product of Sudan I dye during the photocatalytic process. Later, these peaks also started to decrease and diminish at the end, which shows the degradation of formed new degraded products. It can be seen from the last chromatogram at 140 min that there are no peaks present, which supports the degradation of Sudan I.

3.2.5. Cyclic test.

The reusability and stability of the catalyst were tested by performing a cyclic test. For this purpose, the catalyst used in the first cycle was used again for the other cycles without washing it [43]. Figure 8 showed that when the Sn doped CeO_2-Fe_2O_3 photocatalyst was used for the 2nd cycle, it degraded 95 % of the dye, and in its 3rd cycle, the catalyst could degrade up to 93 % of dye from the solution. The efficiency of the Sn doped CeO_2-Fe_2O_3 catalyst was found good even in the 3rd cycle onwards. By performing the cyclic test, the catalyst was found active for the photocatalytic degradation of the dye in consecutive cycles, making it a promising candidate for removing dyes.

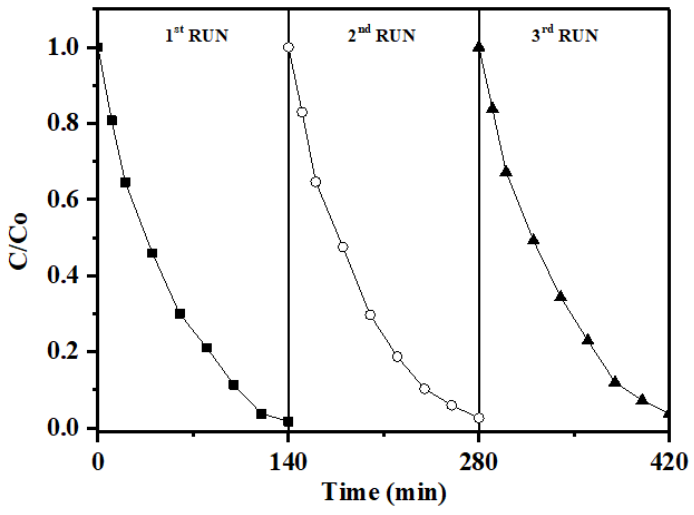

Figure 8. The photocatalytic degradation of Sudan I with Sn doped CeO_2-Fe_2O_3 catalyst up to three consecutive cycles.

3.2.5. Scavenger studies.

The scavenger study was performed to understand the role of reactive species involved in the photocatalytic process. For the scavenger test, the scavengers used are tert-butanol (*t*-BuOH) for $^{\bullet}OH$, benzoquinone (BQ) for $O_2^{\bullet-}$, and ammonium oxalate (AO) for h^+ scavenging [43]. Figure 9 represents the graph for the scavenger study, and it shows that when BQ and *t*-

BuOH were added to the catalyst-dye solution, then the rate of degradation reaction decreased drastically. Still, when AO was added to the reaction then, the degradation rate was not affected. Here, the reason behind it is the formation of $O_2^{\bullet-}$, and $^{\bullet}OH$ radical species during photocatalysis which are responsible for the degradation of dye. And when BQ and t-BuOH were added to the reaction, they scavenged $O_2^{\bullet-}$, and $^{\bullet}OH$ radical species from the reaction and decreased the degradation rate. Figure 9 shows that in the presence of BQ ($O_2^{\bullet-}$ quencher), the reaction proceeds up to 27 %, and in the presence of *t*-BuOH ($^{\bullet}OH$ radical quencher), the reaction proceeds 13 % only. On the other hand, in the presence of AO (h^+ quencher), dye degradation completes up to 98%. So, the scavenger study shows the generation of the $O_2^{\bullet-}$, and $^{\bullet}OH$ radicals as active species for the degradation of Sudan I.

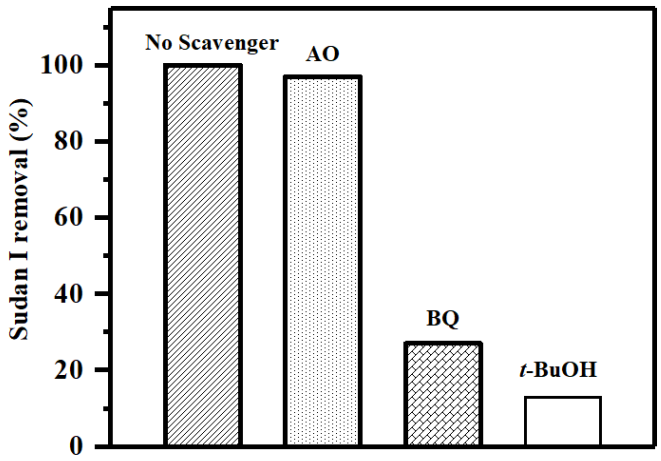

Figure 9. The scavenger studies to understand the role of reactive species on the photocatalytic degradation of Sudan I with Sn doped CeO_2-Fe_2O_3 by using scavengers, BQ, *t*-BuOH, AO.

3.2.6. Mechanism of the photocatalytic degradation process.

Further, the mechanism of the photocatalytic degradation of Sudan I by photocatalyst was studied, and a plausible mechanism is proposed in Figure 10. The photocatalytic process is highly dependent on the bandgap of the catalyst and the availability of the surface charge carriers. In the literature, the bandgap of CeO_2 is reported as 3.1 eV, and for Fe_2O_3, it is 2.3 eV [47,52]. But, here, a new bandgap was achieved by forming a CeO_2 and Fe_2O_3 composite system, which is 2.4 eV. And the doping of Sn in the CeO_2-Fe_2O_3 system leads to the modification in the band gaps, and the new bandgap was 2.21 eV. So, this new bandgap is making the catalyst accessible to visible light uses.

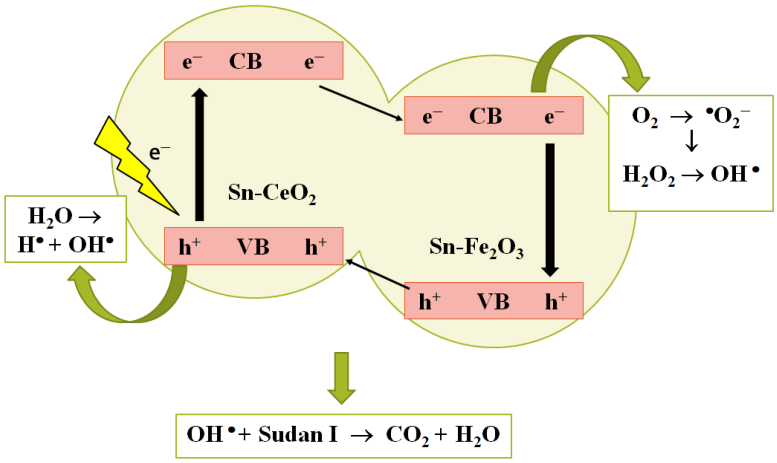

Figure 10. The schematic diagram for the photocatalytic degradation of Sudan I by Sn doped CeO_2-Fe_2O_3 catalyst.

Here, some of the Ce^{4+} lattice sites are occupied by Sn^{4+} ions, which are responsible for the formation of Ce-O-Sn/Fe_2O_3 hetero-junction. It facilitates the migration of the electrons along with the low electron-hole recombination rate [49]. So, the irradiation of catalyst-dye suspension leads to the photogeneration of electrons and holes. These photo-generated electrons move from the valance band (VB) of Sn-CeO_2 to the conduction band (CB) of Sn-CeO_2 and generate holes in the (VB) of Sn-CeO_2. These electrons further move from CB (Sn-CeO_2) to CB (Sn-Fe_2O_3) and then reach the VB (Sn-CeO_2) at the end. These electrons will react with oxygen in the dye solution and convert it into $O_2^{\bullet-}$ radical. These $O_2^{\bullet-}$ radicals will produce $^{\bullet}$OH) by reacting with water molecules, as shown in Figure 10. And the positive holes will also produce $^{\bullet}$OH radicals by the reaction with water molecules present in the solution. The $^{\bullet}$OH radicals react with Sudan I dye and convert it into CO_2 and H_2O molecules through the degradation process [53].

4. Conclusions

In this report, Sn doped CeO_2-Fe_2O_3 nanocomposite is synthesized through a thermal decomposition method and then applied for the photocatalytic degradation of Sudan I dye. The as-synthesized catalyst was characterized by XRD, and it was observed that the doped Sn was well incorporated into the structure, but a shift in 2θ was observed towards the high 2θ values. The FESEM result showed the sphere-shaped morphology of the catalyst in the range of 1-2 μm in size. The surface area of Sn doped CeO_2-Fe_2O_3 and CeO_2-Fe_2O_3 composite was found to be 24.4 and 17 m^2/g, respectively, through the BET analysis. The DRS results showed that Sn doping into the CeO_2-Fe_2O_3 composite led to the bandgap narrowing from 2.4 eV to 2.21 eV. The Sn doped CeO_2-Fe_2O_3 was found to have an improved degradation efficiency than the CeO_2-Fe_2O_3 catalyst. The Sn doped CeO_2-Fe_2O_3 was used to degrade Sudan I under sunlight, and it showed complete degradation of dye within 140 minutes. Degradation of Sudan I was studied by varying different parameters, such as a change in pH and catalyst concentration. Then the reusability of the catalyst was studied by performing a cyclic test, and the catalyst showed good photocatalytic activity up to three consecutive cycles. Further, a suitable mechanism is proposed for the degradation of Sudan I with the transfer of the charge by the catalyst. The COD removal data showed the complete removal of Sudan I from the dye solution by photocatalyst, and HPLC data also supports it. So, the as-synthesized photocatalyst proposed an environment-friendly approach for the degradation of organic dyes, and it can be applied to other organic pollutants in the future.

Funding

This research received no external funding.

Acknowledgments

All authors are grateful to “Genesis of Chemistry” for providing the necessary facilities and support.

Conflicts of Interest

The authors declare no conflict of interest.

References

1. Ledezma, C.Z.; Bolagay, D.N.; Figuera, F.; Ledezma, E.Z.; Ni, M.; Alexis, F.; Guerrero, V.H. Heavy metal water pollution: A fresh look about hazards, novel and conventional remediation methods. *Environ. Technol. Innov*. **2021**, *22*, 101504, https://doi.org/10.1016/j.eti.2021.101504.
2. Liu, J.; Liu, R.; Yang, Z.; Kuikka, S. Quantifying and predicting ecological and human health risks for binary heavy metal pollution accidents at the watershed scale using bayesian networks. *Environ. Pollut.* **2021**, *269*, 116125, https://doi.org/10.1016/j.envpol.2020.116125.
3. Wutich, A.; Rosinger, A.Y.; Stoler, J.; Jepson, W.; Brewis, A. Measuring human water needs. *Am. J. Hum. Biol*. **2020**, *32*, 1-17, https://doi.org/10.1002/ajhb.23350.
4. Haque, M.M.; Haque, M.A.; Mosharaf, M.K.; Marcus, P.K. Decolorization, degradation and detoxification of carcinogenic sulfonated azo dye methyl orange by newly developed biofilm consortia. *Saudi J. Biol. Sci*. **2021**, *28*, 793-804, https://doi.org/10.1016/j.sjbs.2020.11.012.
5. Mohamed, S.H.; Salim, A.I.; Issa, Y.M.; Atwa, M.A.; Nassar, R.H. Evaluation of different sudan dyes in egyptian food samples utilizing liquid chromatography/tandem mass spectroscopy. *Food Anal. Methods*, **2021**, *14*, 2038-2050, http://doi.org/10.1007/s12161-021-02036-x.
6. Abbasi, A.; Ansari, I.I.; Shakir, M. Highly selective and sensitive benzimidazole based bifunctional sensor for targeting inedible azo dyes in red chilli, red food color, trumeric powder, and Cu(Ii) in coconut water. *J. Fluoresc*. **2021**, *31*, 1352-1361, https://doi.org/10.1007/s10895-021-02766-5.
7. Stiborova, M.; Schmeiser, H.H.; Frei, E.; Hodek, P.; Martinek, V. Enzyme oxidizing the azo dye 1-phenylazo-2-naphthol (sudan I) and their contribution to its genotoxicity and carcinogenicity. *Curr. Drug Metab*. **2014**, *15*, 829-840, http://doi.org/10.2174/1389200216666150206125442.
8. Robinson, T.; McMullan, G.; Marchant, R.; Nigam, P. Remediation of Dyes in Textile Effluent: A critical review on current treatment technologies with a proposed alternative. *Bioresour. Technol*. **2001**, *77*, 247-255, https://doi.org/10.1016/S0960-8524(00)00080-8.
9. Govindaraj, M.; Rathinam, R.; Sukumar, C.; Uthayasankar M.; Pattabhi, S. Electrochemical oxidation of bisphenol-a from aqueous solution using graphite electrodes. *Environ. Technol.* **2013**, *34*, 503-511, https://doi.org/10.1080/09593330.2012.701333.
10. Rathinam, R.; Govindaraj, M.; Vijayakumar, K.; Pattabhi, S. Decolourization of rhodamine b from aqueous solution by electrochemical oxidation using graphite electrodes. *Desalination Water Treat*. **2016**, *57*, 16995-17001, https://doi.org/10.1080/19443994.2015.1086960.
11. Saleh, T.A. Protocols for synthesis of nanomaterials polymers, and green materials as adsorbents for water treatment technologies. *Envion. Technol. Innov*. **2021**, *24*, 101821, https://doi.org/10.1016/j.eti.2021.101821.
12. Lum, P.T.; Foo, K.Y.; Zakaria, N.A.; Palaniandy, P. Ash based nanocomposites for photocatalytic degradation of textile dye pollutants: A Review. *Mater. Chem. Phys.* **2020**, *241*, 122405, https://doi.org/10.1016/j.matchemphys.2019.122405.
13. Tsaplin, G.V.; Grishin, S.S.; Baberkina, E.P.; Popkov, S.V.; Talismanov, V.S.; Karmanova, O.G.; Zykova, S.S. Investigation and optimization synthesis pathway of antibacterial drug ethonium. *Rasayan J. Chem*. **2021**, *14*, 1816-1820, http://doi.org/10.31788/RJC.2021.1436574.
14. Inoue, Y. Photocatalytic water splitting by ruo$_2$-loaded metal oxides and nitrides with d^0-and d^{10} –related electronic configurations. *Energy Environ. Sci*. **2009**, *2*, 364-386, https://doi.org/10.1039/B816677N.
15. Rani, M.; Shanker, U. Insight in to sunlight-driven rapid photocatalytic degradation of organic dyes by hexzcyanoferrate-based nanoparticles. *Environ. Sci. Pollut. Res.* **2021**, *28*, 5637-5650, https://doi.org/10.1007/s11356-020-10925-7.
16. Xu, Z.; Shi, Y.; Li, L.; Sun, H.; Amin, M.D.S.; Guo, F.; Wen, H.; Shi, W. Fabrication of 2D/2D Z-scheme highly crystalline carbon nitride/δ-Bi_2O_3 hetero-junction photocatalyst with enhanced photocatalytic degradation of tetracycline. *J. Alloys Compd*. **2022**, *895*, 162667, https://doi.org/10.1016/j.jallcom.2021.162667.
17. Liu, Y.; Zhang, X.; Lu, L.; Ye, J.; Wang, J.; Li, X.; Bai, X.; Wang, W. Nanoplasmonic zirconium nitride photocatalyst for direct overall water splitting. *Chin. Chem. Lett*. **2021**, https://doi.org/10.1016/j.cclet.2021.07.054.
18. Munusamy, S.; Sivaranjan, K.; Sabhapathy, P.; Ramesh, P.S.; Narayanan, V.; Mohammad, F.; Sagadevan, S. Electrochemical and photocatalytic studies of Ta_3N_5-TaON-PEDOT-PANI nanohybrids. *Chem. Phys. Lett*. **2021**, *780*, 138947, https://doi.org/10.1016/j.cplett.2021.138947.

19. Zhang, K.; Guo, L. Metal Sulphide Semiconductors for Photocatalytic Hydrogen Production. *Catal. Sci. Technol*. **2013**, *3*, 1672-1690, https://doi.org/10.1039/C3CY00018D.
20. Munyai, S.; Hintsho-Mbita, N.C. Green derived metal sulphides as photocatalysts for waste water treatment. a review. *Curr. Res. Green Sustain. Chem*. **2021**, *4*, 100163, https://doi.org/10.1016/j.crgsc.2021.100163.
21. Xu, W.; Tian, W.; Li, L. Two-dimentional nanostructured metal oxide/sulfide-based photoanode for photoelectrochemical water splitting. *Sol. RRL*, **2021**, *5*, 2000412, https://doi.org/10.1002/solr.202000412.
22. Mazierski, P.; Mikolajczyk, A.; Bajorowicz, B.; Malankowska, A.; Zaleska-Medynska, A.; Nadolna, J. The role of lanthanides in TiO_2-based photocatalysis: a review. *Appl. Catal. B*: *Environ*. **2018**, *233*, 301-317, https://doi.org/10.1016/j.apcatb.2018.04.019.
23. Yu, J.; Hai, Y.; Jaroniec, M. Photocatalytic hydrogen production over CuO-modified titania. *J. Colloid Interface Sci*. **2011**, *357*, 223-228, https://doi.org/10.1016/j.jcis.2011.01.101.
24. Kayaci, F.; Vempati, S.; Donmez, I.; Biyikli, N.; Uyar, T. Role of zinc interstitials and oxygen vacancies of zno in photocatalysis: a bottom-up approach to control defect density. *Nanoscale*, **2014**, *6*, 10224-10234, https://doi.org/10.1039/C4NR01887G.
25. Umadevi, M.; Rathinam, R.; Poornima, S.; Santhi, T.; Pattabhi, S. Electrochemical degradation of reactive red 195 from its aqueous solution using $RuO_2/IrO_2/TaO_2$ coated titanium electrodes. *Asian J. Chem*. **2021**, *33*, 1919-1922, http://dx.doi.org/10.14233/ajchem.2021.23330.
26. Rathinam, R.; Govindaraj, M. Photoelectrocatalytic oxidation of textile industry wastewater by $RuO_2/IrO_2/TaO_2$ coated titanium electrodes. *Nat. Environ. Pollut. Technol*. **2021**, *20*, 1069-1076, https://doi.org/10.46488/NEPT.2021.v20i03.014.
27. Sabry, R.S.; Rahmah, M.I.; Aziz, W.J. A systematic study to evaluate effect of stearic acid on superhydrophobicity and photocatalytic properties of Ag-doped ZnO nanostructures. *J Mater Sci*: *Mater. Electron*. **2020**, *31*, 13382-13391, https://doi.org/10.1007/s10854-020-03893-8.
28. Kayani, Z.N.; Usman, A.; Nazli, H.; Sagheer, R.; Riaz, S.; Naseem, S. Dielectric and magnetic properties of dilute magnetic semiconductors Ag-doped ZnO thin films. *Appl. Phys. A*, **2020**, *126*, 1-10, https://doi.org/10.1007/s00339-020-03748-3.
29. Majumder, D.; Chakraborty, I.; Mandal, K.; Roy, S. Facet-dependent photodegradation of methylene blue using pristine CeO_2 nanostructures. *ACS Omega*, **2019**, *4*, 4243-4251, https://doi.org/10.1021/acsomega.8b03298.
30. Channei, D.; Nakaruk, A.; Jannoey, P.; Phanichphant, S. Preparation and characterization of Pd modified CeO_2 nanoparticles for photocatalytic degradation of dye. *Solid State Sci*. **2019**, *87*, 9-14, https://doi.org/10.1016/j.solidstatesciences.2018.10.016.
31. Yang, Z.M.; Huang, G.F.; Huang, W.Q.; Wei, J.M.; Yan, X.G.; Liu, Y.Y.; Jiao, C.; Wan, Z.; Pan, A. Novel Ag_3Po_4/CeO_2 composite with high efficiency and stability for photocatalytic applications. *J. Mater. Chem. A*, **2014**, *2*, 1750-1756, https://doi.org/10.1039/C3TA14286H.
32. Wetchakun, N.; Chaiwichain, S.; Inceesungvorn, B.; Pingmuang, K.; Phanichphant, S.; Minett, A.I.; Chen, J. $BiVO_4/CeO_2$ nanocomposites with high visible-light-induced photocatalytic activity. *ACS Appl. Mater. Interfaces*, **2012**, *4*, 3718-3723, https://doi.org/10.1021/am300812n.
33. Hu, S.; Zhou, F.; Wang, L.; Zhang, J. Preparation of Cu_2O/CeO_2 hetero-junction photocatalyst for the degradation of acid orange 7 under visible light irradiation. *Catal. Commun*. **2011**, *12*, 794-797, https://doi.org/10.1016/j.catcom.2011.01.027.
34. Krishnan, A.; Beena, S.; Chandran, M. Fabrication and evaluation of CeO_2-Fe_2O_3 mixed oxide for hydrogen evolution by photo water splitting reaction under visible light irradiation. *Mater. Today*: *Proc*. **2019**, *18*, 4968-4976, https://doi.org/10.1016/j.matpr.2019.07.489.
35. Liu, H.; Shon, H.K.; Sun, X.; Vigneswaran, S.; Nan, H. Preparation and characterization of visible light responsive Fe_2O_3-TiO_2 composites. *Appl. Surf. Sci.* **2011**, 257, 5813-5819, https://doi.org/10.1016/j.apsusc.2011.01.110.
36. Hassan, S.M.; Ahmed, A.I.; Mannaa, M. A. Preparation and characterization of SnO_2 doped TiO_2 nanoparticles: effect of phase change on the photocatalytic and catalytic activity. *J. Sci*: *Adv. Mater*. and *Dev*. **2019**, *4*, 400-412, https://doi.org/10.1016/j.jsamd.2019.06.004.
37. Sohail, M.; Baig, N.; Sher, M.; Jamil, R.; Altaf, M.; Akhtar, S.; Sharif, M. A novel tin-doped titanium oxide nanocomposite for efficient photo-anodic water splitting. *ACS Omega*, **2020**, *5*, 6405-6413, https://doi.org/10.1021/acsomega.9b03876.
38. Alwera, S.; Bhushan, R. RP-HPLC enantioseparation of β–adresnolytic using miceller mobile phase without organic solvents. *Biomed. Chromatogr*. **2017**, *31*, e3983 (1-7), https://doi.org/10.1002/bmc.3983.

39. Alwera, V.; Sehlangia, S.; Alwera, S. A Sensitive micellar liquid chromatographic method for the rectification of enantiomers of esmolol, and determination of absolute configuration and elution order. *J. Liq. Chromatogr. Relat. Technol*. **2020**, *43*, 742-749, https://doi.org/10.1080/10826076.2020.1798250.
40. Krishnan, A.; Shibli, S.M.A. In situ surface decoration of a titanium nanosubstrate by a TiO_2-WO_3 composite. *Ind. Eng. Chem. Res*. **2018**, *57*, 16217-16226, https://doi.org/10.1021/acs.iecr.8b03692.
41. Bhagya, T.C.; Krishnan, A.; Rajan S.A.; Sha M.A.; Sreelekshmy, B.R.; Jineesh, P.; Shibli, S.M.A. Exploration and evaluation of proton source-assisted photocatalyst for hydrogen generation. *Photochem. Photobiol. Sci*. **2019**, *18*, 1716-1726, https://doi.org/10.1039/C9PP00119K.
42. Abhilash, M.R.; Akshatha, G.; Srikantaswamy, S. Photocatalytic dye degradation and biological activities of the Fe_2O_3/Cu_2O nanocomposite. *RSC Adv*. **2019**, *9*, 8557–8568, https://doi.org/10.1039/C8RA09929D.
43. Alwera, V.; Singh, S.; Srivastava, V.C.; Mandal, T.K. Manganese trioxide with various morphologies: applications in catalytic dye degradation. *Chemistry Select*, **2020**, *5*, 4674-4684, https://doi.org/10.1002/slct.202000298.
44. Chen, L.C.; Tu, Y.J.; Wang, Y.S.; Kan, R.S.; Huang, C.M. Characterization and photoreactivity of N-, S-, and C-doped ZnO under uv and visible light illumination. *J. Photochem. Photobiol. A*: *Chem*. **2008**, *199*, 170-178, https://doi.org/10.1016/j.jphotochem.2008.05.022.
45. Lahmar, H.; Benamira, M.; Douafer, S.; Messaadia, L.; Boudjerda, A.; Trari, M. Photocatalytic degradation of methyl orange on the novel hetero-system La_2NiO_4/ZnO under solar light. *Chem. Phys. Lett.* **2020**, *742*, 137132, https://doi.org/10.1016/j.cplett.2020.137132.
46. Eskizeybek, V.; Sarı, F.; Gülce, H.; Gülce, A.; Avcı, A. Preparation of the new polyaniline/ZnO nanocomposite and its photocatalytic activity for degradation of methylene blue and malachite green dyes under UV and natural sun lights irradiations. *Appl. Catal. B*: **2012**, *119*, 197-206, https://doi.org/10.1016/j.apcatb.2012.02.034.
47. Prabhu, S.; Viswanathan, T.; Jothivenkatachalam, K.; Jeganathan, K. Visible Light photocatalytic activity of CeO_2-ZnO-TiO_2 composites for the degradation of rhodamine b. *Ind. J. Mat. Sci.* **2014**, *2014*, 536123, http://dx.doi.org/10.1155/2014/536123.
48. Boughelout, A.; Macaluso, R.; Kechouane, M.; Trari, M. Photocatalysis of rhodamine b and methyl orange degradation under solar light on ZnO and Cu_2O thin films. *Reac. Kinet. Mech. Cat*. **2020**, *129*, 1115-1130, https://doi.org/10.1007/s11144-020-01741-8.
49. Anwer, H.; Mahmood, A.; Lee, J.; Kim, K.H.; Park, J.W.; Yip, A.C.K. Photocatalytsts for degradation of dyes in industrial effluents: opportunities and challenges. *Nano Res.* **2019**, *12*, 955-972, https://doi.org/10.1007/s12274-019-2287-0.
50. Alwera, S.; Bhushan, R. (*RS*)-Propranolol: Enantioseparation by HPLC using newly synthesized (*S*)-levofloxacin-based reagent, absolute configuration of diasteromers and recovery of native enantiomers by detagging. *Biomed. Chromatogr*. **2015**, *30*, 1223-1233, https://doi.org/10.1002/bmc.3671.
51. Alwera S. In Situ derivatization of (*RS*)-mexiletine and enantioseparation using micellar liquid chromatography: a green approach. ACS *Sustainable Chem. Eng*. **2018**, *6*, 11653-11661, https://doi.org/10.1021/acssuschemeng.8b01869.
52. Bandara, J.; Klehm, U.; Kiwi, J. Raschig rings-Fe_2O_3 composite photocatalyst activate in the degradation of 4-chlorophenol and orange ii under daylight irradiation. *Appl. Catal. B*, **2007**, *76*, 73-81, https://doi.org/10.1016/j.apcatb.2007.05.007.
53. Zha, R.; Nadimicherla, R.; Guo, X. Ultraviolet photocatalytic degradation of methyl orange by nanostructured TiO_2/ZnO hetero-junctions. *J. Mater. Chem. A*., **2015**, *3*, 6565-6574, https://doi.org/10.1039/C5TA00764J.